Effect of celestial body gravity on Taiji mission range and range acceleration noise

Xiaoqing Han,[1,2] Xiaodong Peng,[1,3,4,5] Wenlin Tang,[1,*] Zhen Yang,[1] Xiaoshan Ma,[1] Chen Gao,[1] Li-e Qiang,[1] Yuzhu Zhang,[1] Mengyuan Zhao,[1,2] Jiafeng Zhang,[1,2] and Binbin Liu[1,2]

[1]*Key Laboratory of Electronics and Information Technology for Space System, National Space Science Center, Chinese Academy of Sciences, Beijing 100190, China*
[2]*University of Chinese Academy of Sciences, Beijing 100049, China*
[3]*School of Fundamental Physics and Mathematical Sciences, Hangzhou Institute for Advanced Study, UCAS, Hangzhou 310024, China*
[4]*Taiji Laboratory for Gravitational Wave Universe, Hangzhou 310024, China*
[5]*Key Laboratory of Gravitational Wave Precision Measurement of Zhejiang Province, Hangzhou 310024, China*

(Received 18 March 2022; revised 14 September 2022; accepted 21 October 2022; published 18 November 2022)

The Taiji project is a space gravitational-wave detection mission consisting of three satellites that form a giant equilateral triangle with a side length of approximately 3×10^6 km in the heliocentric orbit. The target of the mission is to detect gravitational-wave signals in the 0.1 mHz to 1 Hz band. However, its intersatellite distances are affected by celestial bodies in the solar system, introducing changes that may reach levels of 30,000 km in magnitude. Thus, it is important to investigate whether the gravitational fields of celestial bodies in the detection frequency band will have an impact on the realization of ultrahigh-sensitivity intersatellite ranging measurements. In this study, a high-precision orbit propagator with an accuracy of 0.03 pm on the 1 AU scale is developed. Based on this orbit propagator, the impact of the major large celestial bodies in the solar system on the detection sensitivity in the intersatellite measurements are analyzed. Detailed numerical studies show that the linear spectral density of the range and range acceleration are approximately 1×10^{-13} m/$\sqrt{\text{Hz}}$ and 5×10^{-23} m/s^2/$\sqrt{\text{Hz}}$, respectively, at 0.1 mHz, indicating that the gravitational disturbance generated by the major celestial bodies in the solar system will not affect the aim of the Taiji mission to detect gravitational waves in the frequency band 0.1 mHz to 1 Hz.

DOI: 10.1103/PhysRevD.106.102005

I. INTRODUCTION

Taiji is a space gravitational-wave antenna proposed by the Chinese Academy of Sciences to detect gravitational waves in the frequency band 0.1 mHz to 1 Hz [1]. The antenna consists of three satellites configured in a giant equilateral triangle satellite formation with a side length of approximately 3×10^6 km. The satellites move in a heliocentric orbit, i.e., centered on the Sun, whereas the mass center of the satellite formation moves in a circular orbit around the Sun, which falls on the Earth orbit and trails Earth for 20° or −20° [2]. Each satellite, which contains two laser-interferometric ranging systems and two drag-free control systems, interferes with the other two to form three Michelson-type interferometers. To detect weak gravitational-wave (GW) signals, the drag-free control systems provide an ultra-stable satellite platform and a sub-femto-g inertial reference for the laser ranging interferometers. The laser interferometers need to reach picometer precision to detect weak GW signals. According to the baseline design of the Taiji mission [3], the range measurement accuracy of the laser system is approximately 8×10^{-12} m/$\sqrt{\text{Hz}}$ around 0.01 Hz, whereas the residual acceleration noise along the sensitive axis is approximately 3×10^{-15} m/s^2/$\sqrt{\text{Hz}}$ in the vicinity of 0.01 Hz.

Based on the ultrahigh laser ranging accuracy and ultralow microgravity level requirements of Taiji, several sources of disturbances should be considered in the mission design. Among these sources of disturbances, the space environment is one of the most important. Space environment may be divided into two types: one is the gravitational environment of celestial bodies in the solar system, and the other is the space environment excluding celestial gravity, which includes solar radiation pressure, interplanetary magnetic field, and plasma, among others. With regard to the second type of space environment, its influence on space gravitational-wave detection may be suppressed based on a combination of strategies for isolation, sensing, and control to keep a pair of PMs in each of the three spacecrafts close to a free-fall (inertial) condition as possible ([4,5,6]).

*Corresponding author.
tangwenlin@nssc.ac.cn

The influence of celestial bodies concerns two aspects of the mission. First, the influence of celestial bodies determines the orbit and stability of the satellite formation, which further determine the technical requirements of the core payloads. For example, the relative velocity between two satellites is critical to the design of the dynamic range of the phase meter [7] and the laser frequency plan [8,9], whereas the breathing angle between two arms determines the dynamic range requirement of the pointing adjustment mechanism [10]. Second, because the disturbance reduce system cannot reduce the gravitational force generated by the gravitational fields of celestial bodies [11], then, in theory, we cannot distinguish whether changes in the distance (or the arm length) between two satellites are caused by the gravitational fields of celestial bodies or by gravitational waves.

For the Taiji mission, changes in the arm length due to the gravitational fields of celestial bodies can be approximately 1% of the initial arm length, or approximately 30,000 km, which far exceeds the gravitational wave observation signal in magnitude. Therefore, it is necessary to study whether variations in the distance between two satellites caused by celestial gravity exceed the gravitational wave observation signal in the detection frequency band.

Because the orbit of Taiji is similar to that of the first proposed space-borne gravitational wave detection mission LISA (Laser Interferometer Space Antenna) [6], we may borrow from the results of past studies that analyzed the influence of celestial bodies on the detection of gravitational waves in the heliocentric orbit. For the LISA mission, scientists analytically studied the influences of the Earth–Moon system and of other celestial bodies. The main effect on the distance variation caused by the Earth–Moon system is in a very low-frequency range, from 3×10^{-8} Hz to about 2×10^{-6} Hz, and it is estimated that, in the detection band, the influence is less than that caused by the laser ranging noise. Other planets have even less influence [12]. However, the aforementioned results were obtained via semi-analytical analysis. Because the gravitational effects of celestial bodies are coupled with each other, it will be useful to estimate the influence of these celestial bodies through numerical simulation.

To analyze the influence of celestial bodies on the Taiji mission, we will need to solve two difficult problems. The first problem is that the spatial scale in the orbit simulation of Taiji is at least 24 orders in magnitude. Thus, a high-precision numerical simulation spanning 0.1 pm to 1 AU is required. Currently, for a number of space missions, such as the Grace Follow-On [13] and Tianqin [14] missions, high-precision numerical computing methods have already been developed. However, the spans of their spatial scales are not as wide as that of Taiji (or of LISA), and thus their orbit calculations do not consider ranges as wide as that of the Taiji mission. Thus, we need to develop a high-precision orbit propagator with an accuracy of approximately 0.1 pm in the 1 AU scale. In this respect, we will learn from the process of developing the high-precision orbit integrator for the Grace Follow-On mission. In this study, we will develop a high-precision orbit propagator based on the high-precision calculation library Multiple Precision Floating-Point Reliable (MPFR) [15] Library and the ordinary differential equation solver DOP853 [16]. With this orbit propagator, and using 34 significant digits, we may realize an orbit calculation with a high precision of approximately 0.03 pm in the 1 AU scale over a duration of six years using the two-body problem as the verification model.

The second problem is that when we analyze the gravitational effects of celestial bodies in the frequency domain, the frequency band ranges from the orbit frequency, which is approximately 3×10^{-8} Hz, to the detection frequency of Taiji, which ranges from 0.1 mHz to 1 Hz. The range of the amplitude of the spectrum is from the subpicometers to several tens of thousands of kilometers. Thus, a very high frequency resolution with a wide dynamic range of amplitude is needed in the spectral analysis. However, the orbital period of the Taiji mission is approximately 1 year, and its mission duration of 6 years is equivalent to only approximately six periods. This limited number of periods will have a significant influence on the selection of window functions for the spectral analysis. In our study, we will search for suitable window functions, which will be verified based on the analysis of the two-body problem. Then, using the selected window functions, we will estimate the upper bound of the influences of the central gravity of the Sun, the major celestial bodies in the solar system, and the 344 small celestial bodies outlined in the Jet Propulsion Laboratory (JPL) calendar DE430 [17] on the range and range acceleration among the satellites in the detection band.

Because LISA has the same orbital position as that of the Taiji program and has a slightly shorter arm length of approximately 2.5 million kilometers, the analysis results of this study are also applicable to LISA.

The outline of this paper is as follows. Section II describes the requirements relevant to the detection accuracy of Taiji. Section III introduces the high-precision satellite orbit propagator, for which the two-body problem is used to verify correctness and accuracy. Section IV introduces the force model and initial orbit parameters of the Taiji mission, and presents the results of a spectral analysis of the range and range acceleration caused by celestial bodies. Lastly, the final section of this paper presents the conclusions of the study.

II. ACCURACY REQUIREMENTS

The requirements for the accuracy of numerical simulation of the orbits of Taiji may be derived from the baseline design of the Taiji mission, which is shown in Table I [2]. To estimate the influence of the gravitational fields of celestial bodies, the accuracy of numerical simulation should be at

TABLE I. Taiji mission requirements [2].

Mission	Frequency band	Ranging accuracy	Acceleration noise	Orbit radius
Taiji	0.1 mHz–1 Hz	8 pm/Hz$^{1/2}$	3×10^{-15} ms^{-2}/Hz$^{1/2}$	≈1 AU

least one order of magnitude higher than the requirements shown in Table I.

The intersatellite observations concerned include the arm length (range), range rate, and range acceleration. They require different numbers of significant digits in the numerical calculation because of their different dynamic ranges in magnitude. The range between two satellites is defined by

$$L_{12} = |\vec{r}_2 - \vec{r}_1|, \tag{1}$$

where $\vec{r}_1$ and $\vec{r}_2$ are the position vectors of satellite 1 and satellite 2 in the inertial reference system, respectively, relative to the center of the Sun. In our study, we will use the heliocentric ecliptic coordinate system of J2000.0 (denoted by HECSJ2000) as the inertial reference system. The positions of the satellites are approximately 1 AU, or $\approx 1.496 \times 10^{11}$ m, in magnitude, whereas the variation in the arm length needs to be measured in the order of several picometers. Therefore, the numerical representation of the arm length observation requires at least 23 significant digits, which is far beyond the current range of double-precision values, or 16 significant digits. The range rate may be obtained from the derivative of the range as

$$\dot{L}_{12} = \frac{\vec{r}_2 - \vec{r}_1}{L_{12}} \cdot (\dot{\vec{r}}_2 - \dot{\vec{r}}_1) = \vec{e}_{12} \cdot (\dot{\vec{r}}_2 - \dot{\vec{r}}_1), \tag{2}$$

where $\vec{e}_{12} = (\vec{r}_2 - \vec{r}_1)/L_{12}$ is the unit direction vector from satellite 1 to satellite 2. The speeds of the satellites in Taiji are approximately 3×10^4 m/s in magnitude. The requirement for the range rate may be obtained from that for range, such as $2\pi f \tilde{L}(f)$ (where $\tilde{L}(f)$ is the ranging accuracy, as shown in Table I), which is approximately 6.28×10^{-14} m/s/$\sqrt{\text{Hz}}$ (based on $2\pi f \times 10^{-12}$ m/$\sqrt{\text{Hz}}$ at $f = 0.01$ Hz). Thus, the numerical representation of $\dot{L}_{12}$ requires at least 18 significant digits. Finally, that for the range acceleration can be obtained from the derivative of the range rate as

$$\begin{aligned}\ddot{L}_{12} &= \frac{\vec{r}_2 - \vec{r}_1}{L_{12}} \cdot (\ddot{\vec{r}}_2 - \ddot{\vec{r}}_1) + \frac{1}{L_{12}} \cdot (|\dot{\vec{r}}_2 - \dot{\vec{r}}_1|^2 - \dot{L}_{12}^2) \\ &= \vec{e}_{12} \cdot (\ddot{\vec{r}}_2 - \ddot{\vec{r}}_1) + \frac{1}{L_{12}} \cdot (|\dot{\vec{r}}_2 - \dot{\vec{r}}_1|^2 - \dot{L}_{12}^2).\end{aligned} \tag{3}$$

The range acceleration of the Taiji satellite due to the gravitational fields of celestial bodies is in the order of 1×10^{-6} m/s^2, whereas the required limit for the residual acceleration noise is 3×10^{-15} m/s^2/$\sqrt{\text{Hz}}$. Thus, the numerical representation of $\ddot{L}_{12}$ requires at least 9 significant digits.

TABLE II. Dynamic range of intersatellite observations.

Inter-satellite observations	Dynamic range
Range	10^{-12}–10^{11}
Range rate	10^{-14}–10^{4}
Range acceleration	10^{-15}–10^{-6}

The dynamic ranges of these three intersatellite observations are summarized in Table II. Based on all of these findings thus far, at least 23 significant digits are required to precisely represent the intersatellite observations of Taiji.

III. HIGH-PRECISION ORBIT PROPAGATOR

To evaluate the effect of celestial gravitational fields on intersatellite range and range acceleration, we need high-precision models of the gravitational fields and high-precision numerical simulations of the satellite orbits. In this section, we will introduce the high-precision orbit propagator that we use in this study.

In the simulation, the error of the numerical integration of the orbit needs to be maintained at least one order of magnitude smaller than the required limits outlined in Table I, to safely avoid contamination [18]. In our study, the required accuracies for the position and acceleration implemented in our numerical simulation are approximately 0.1 pm and 1×10^{-16} m/s^2, respectively. Meanwhile, the effect of accumulating errors should also be considered in this simulation, and thus, 1–3 additional significant digits are required to cover the dynamic range shown in Table I. Furthermore, considering the general high-precision requirements of future deep space exploration missions, we develop a high-precision orbit propagator that can implement an arbitrary number of significant digits for floating-point arithmetic (limited only by the available memory).

A. High-precision orbit propagator with arbitrary number of significant digits

MPFR is an open-source library that can be used to perform floating-point operations with arbitrary numbers of significant digits (limited only by the available memory). It provides the fundamental mathematical functions sin, sqrt, pow, log, etc. The framework of a high-precision orbit propagator with arbitrary number of significant digits is

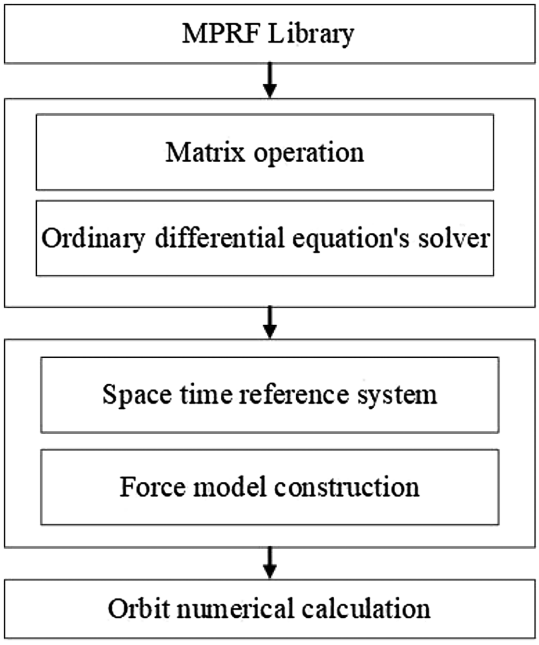

FIG. 1. Framework of orbit propagator.

shown in Fig. 1. First, based on the MPFR, we develop a matrix operation and an ordinary differential equation solver. Afterward, we develop a space–time reference system and a force model of the gravitational fields. Finally, we derive the numerical calculation of the orbit and perform the relevant spectral analysis.

The ordinary differential equation solver that we use in this study is the famous 8th-order variable-step Runge–Kutta integrator DOP853. For the number of significant digits, it will be a trade-off between resource management and time performance. Based on the findings of past research on using quadruple-precision [14,19,20], we use 34 significant digits in calculating the orbit.

B. Accuracy evaluation

It is well known that the accuracy of an orbit integrator may be evaluated based on comparisons of the numerical calculation of the orbit with its analytical solution, using the two-body problem [19]. The state of a satellite can be represented using Kepler orbit elements [21], namely, semimajor axis (a), eccentricity (e), orbit inclination (i), right ascension of ascending node (Ω), argument of perigee (ω), and mean anomaly (M). The position of a satellite in HECSJ2000 is given by [22]

$$\vec{R} = R_3(-\Omega)R_1(-i)R_3(-\omega)\begin{bmatrix} a(\cos E - e) \\ a\sqrt{1-e^2}\sin E \\ 0 \end{bmatrix}, \quad (4)$$

where the functions $R_1(\cdots)$ and $R_3(\cdots)$ are the Euler rotation matrices around the x and z axes, respectively, whereas E is the eccentric anomaly, which can be calculated using the Kepler equation [22]

$$E - e\sin E = M. \quad (5)$$

The mean anomaly at the epoch t can be solved using the following formula:

$$M = M_0 + n(t - t_0), \quad (6)$$

where $n = \sqrt{\mu/a^3}$ is the angular velocity of the orbit, μ is the gravitational parameter of the central body, t_0 is the initial time, and M_0 is the mean anomaly at the initial time. The velocity vector $\vec{V}$ of the satellite is given by the following formula [22]:

$$\vec{V} = \frac{na}{1 - e\cos E}R_3(-\Omega)R_1(-i)R_3(-\omega)\begin{bmatrix} -\sin E \\ \sqrt{1-e^2}\cos E \\ 0 \end{bmatrix}. \quad (7)$$

In our study, we use the ideal "Sun–Earth" two-body problem to verify our integrator. The reason for this selection is that the distance between Earth and the Sun is approximately 1 AU, and thus it has the same spatial scale as that of Taiji. The equation of motion of the two-body problem is

$$\ddot{\vec{r}} = -\frac{\mu_S}{|\vec{r}|^3}\cdot\vec{r}, \quad (8)$$

where $\vec{r}$ is the position of Earth, and $\mu_S = GM_S$ is the gravitational parameter of the Sun. We also select midnight on January 1, 2030, as the initial moment. To summarize, the initial orbit elements are outlined in Table III.

The numerical solution is obtained via numerical integration with the 8th-order variable-step DOP853 integrator, and the analytical solution is obtained according to Eqs. (4) and (7). When the integral orbit is subtracted from the analytic orbit, the difference can be used to evaluate the accuracy level of the numerical integration, which is expressed in HECSJ2000.

TABLE III. Initial Kepler orbit elements of Earth in 2030.01.01.

Orbit elements	Initial value
a (m)	$1.4959788521179774500000000000000000 \times 10^{11}$
e	$1.6698808000000000000000000000000000 \times 10^{-2}$
i (rad)	$-6.7398797947847693828869858509801 93 \times 10^{-2}$
Ω (rad)	6.06013814834975750442892081919735 0
ω (rad)	2.02155740761941003564939080462 1808
M (rad)	6.23482262630590530307288610319 4597

The error tolerance, which is determined empirically after several trials, is set to 1×10^{-26}. The integration period is six years, spanning January 1, 2030, to January 1, 2036, which is consistent with the expected mission duration of Taiji. Moreover, the selection of different time periods has no subversive impact on the accuracy evaluation of the results. The sampling interval is set to one day.

Figure 2 shows the differences in the three components of the position vector obtained from the numerical integration and the analytical solution. From these results, it can be clearly observed that when the error tolerance of the DOP853 solver is set to 1×10^{-26}, the maximum position error within six years is within 3×10^{-14} m, or 0.03 pm, which fulfills the expected accuracy. Figure 3 shows the difference between the numerical integration and analytical solution of the three components of the velocity. The maximum difference is within 5×10^{-21} m/s, which also fulfills the requirement.

To sum up, it can be inferred that when the error tolerance is set to 1×10^{-26}, the maximum position error and maximum velocity error obtained using the 8th-order variable-step DOP853 algorithm for a mission duration of six years satisfy the requirements. Thus, the integrator based on 34 significant digits is sufficient for accurately simulating the Taiji intersatellite observations. In the subsequent parts of the study, we will use this integrator with an error tolerance of 1×10^{-26} to calculate the orbits of the Taiji satellites, and then perform a reliable spectral analysis of the Taiji range and range acceleration while accounting for the effects of the gravitational fields of celestial bodies.

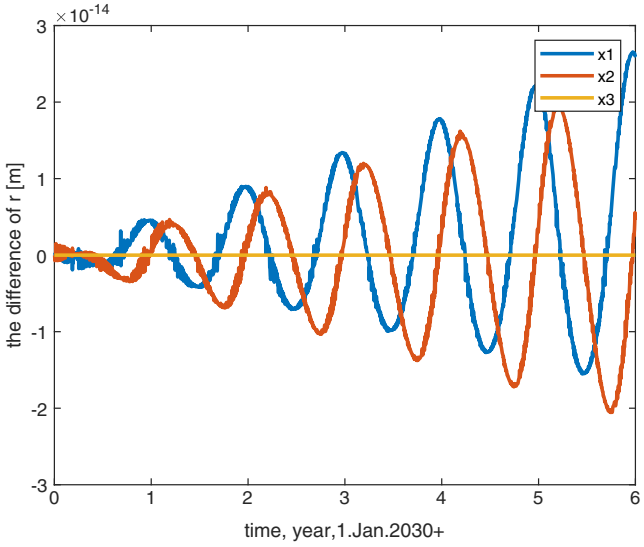

FIG. 2. Differences in three components of position between numerical integration and analytical solution.

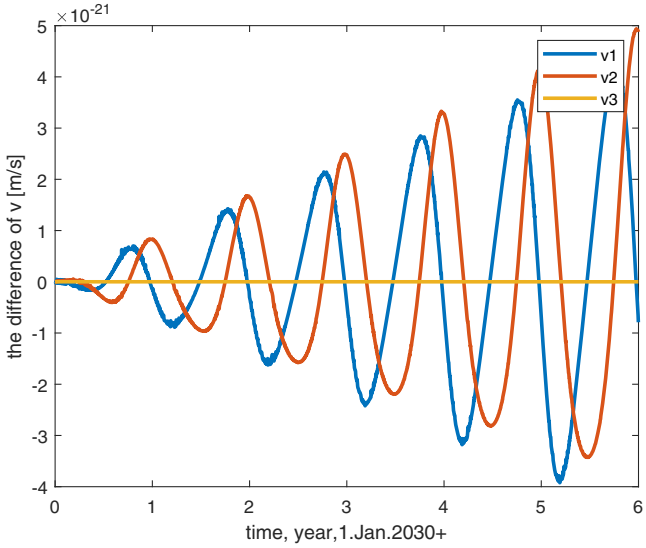

FIG. 3. Differences in three components of velocity between numerical integration and analytical solution.

IV. NUMERICAL SIMULATION OF TAIJI'S ORBIT AND ITS SPECTRUM ESTIMATION

A. Force model and orbital parameter settings

Because our goal is to evaluate the influence of the gravitational fields of celestial bodies on the range and range acceleration, we consider only the Newtonian gravitational forces of the Sun and of the ten other major bodies in the solar system-Mercury, Venus, Earth, Mars, Jupiter, Saturn, Uranus, Neptune, Pluto and Moon. The equation of motion of the satellites may be written in HECSJ2000 as

$$\ddot{\vec{r}}_j = -\mu_S \frac{\vec{r}_j}{r_j^3} - \sum_p \mu_p \left(\frac{\vec{r}_j - \vec{R}_p}{|\vec{r}_j - \vec{R}_p|^3} + \frac{\vec{R}_p}{\vec{R}_p^3} \right), \tag{9}$$

where μ_S and μ_p represent the gravitational parameters of the Sun and planets, respectively; and $\vec{r}_j$ and $\vec{R}_p$ represent the positions of the jth satellite and planet, respectively. The positions of the planets are provided by the JPL planetary ephemeris DE430 in our work. The initial conditions of the orbit, which are obtained from the Ref. [23], are shown in Table IV.

B. Effect of the Sun

Because the gravitational field of the Sun is the most significantly influential among all the celestial bodies in the solar system, we first use the analytical solution Eqs. (4) and (7) of the two-body problem to calculate the states of the three satellites when only the central gravitational field of the Sun is considered, after which we perform a spectral analysis of the intersatellite range and range accelerations. In this case, the orbital period of the

TABLE IV. Initial Kepler orbit elements of three satellites in 2030.01.01.

Orbit elements	SC1	SC2	SC3
a (m)	1.4959634565681490386 58328221198078 × 10^{11}	1.4959655899222014199 90617423675783 × 10^{11}	1.4959697193924532455 97536941283611 × 10^{11}
e	5.7765668488692236856 47181406043320 × 10^{-3}	5.7787542595113695371 10531279492637 × 10^{-3}	5.7800535062226950242 26810413151545 × 10^{-3}
i (rad)	4.1885699049577268650 87121482595773 × 10^{-1}	4.0563848156460195492 88806113694051 × 10^{-1}	4.0266269238196154535 13913766115822 × 10^{-1}
Ω (rad)	6.2789100176769823 75829771717787871	2.3694187073916838473 22118615655240 × 10^{-2}	6.2634647123248397 47701881516419234
ω (rad)	4.5455776282658893 41560697014080119	3.3140211927096511153 63630142379896 × 10^{-1}	2.4647099564304789 72887554769833421
M (rad)	3.1415926535897932 38462643383279503	1.0469124253667905 41597336550216426	5.2366647183200991 85998260190091934

satellite can be calculated to be approximately $T = 365.2568983$ days, and the orbital frequency to be approximately $f_0 = 3.1687489 \times 10^{-8}$ Hz.

The linear spectrum of a signal $\{x_k\}$ may be obtained from its discrete Fourier transform (DFT). Using the window function $\{w_k\}$, the DFT of $\{w_k x_k\}$ is defined by [24]

$$y_m = \sum_{k=0}^{N-1} w_k x_k \exp\left(-i2\pi \frac{mk}{N}\right), \quad m = 0, \ldots, N-1. \tag{10}$$

Then the linear spectrum of $\{x_k\}$ is estimated to be [24]

$$LS(f_m = m \cdot f_{\text{res}}) = \frac{2}{S_1}|y_m|, \quad m = 0, \ldots, \frac{N}{2}, \tag{11}$$

where $f_{\text{res}} = fs/N$ is the frequency resolution, fs is the sampling frequency and S_1 is defined to be

$$S_1 = \sum_{j=0}^{N-1} w_j. \tag{12}$$

The linear spectral density of $\{x_k\}$ is estimated to be [24]

$$LSD(f_m = m \cdot f_{\text{res}}) = 2\sqrt{\frac{1}{f_s S_2}}|y_m|, \quad m = 0, \ldots, \frac{N}{2}, \tag{13}$$

where S_2 is defined to be

$$S_2 = \sum_{j=0}^{N-1} w_j^2. \tag{14}$$

1. How to choose the window functions

In this section, we explain how the window function is chosen. When only the central gravitational field of the Sun is considered, the intersatellite ranges are periodic with the orbital period when the three spacecrafts have the same semimajor axes. The choice of window function depends on whether the duration of the sampling is an integer multiple of the orbital period.

Here, we will consider two situations, the first one is a coherent sampling whose duration of the sampling is greater than that of the orbital period by a factor of six. The second one is a noncoherent sampling whose duration of sampling is not an integer multiple of the orbital period.

In the first situation, the duration of the sampling is six periods, namely, $6T$. The sampling interval Δt is set to approximately 49.9999937 s such that the duration of the sampling $N\Delta t$, with N = 3786984, yields exactly 6 orbital periods of data to analyze. The orbit is solved based on 34 significant digits. Given the orbit, the range and range acceleration are calculated. Without loss of generality, we analyze only the range L_{12}^{Sun} and range acceleration $\ddot{L}_{12}^{\text{Sun}}$ between satellites 1 and 2, which are shown in Figs. 4 and 5, respectively. From these two figures, it is clear that the

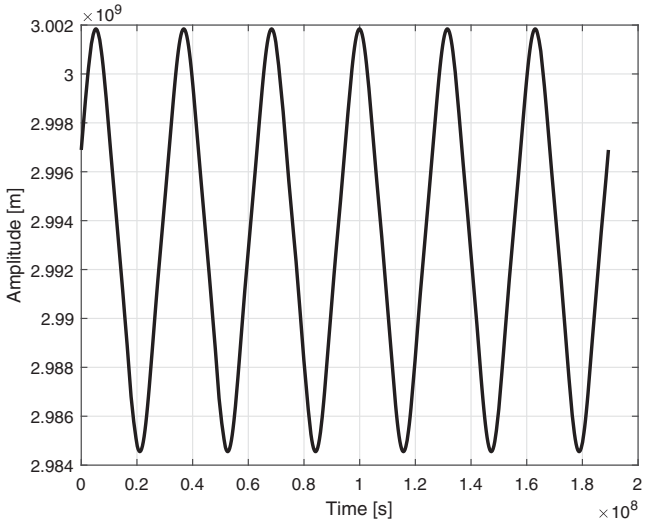

FIG. 4. Simulated time series of L_{12}^{Sun}.

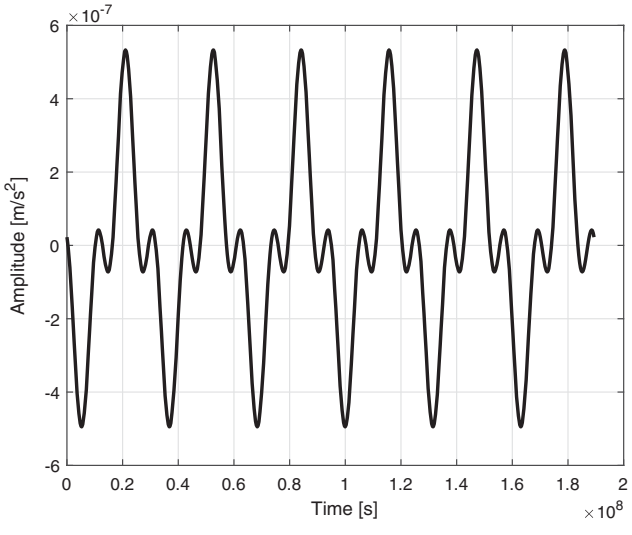

FIG. 5. Simulated time series of $\ddot{L}_{12}^{\mathrm{Sun}}$.

maximum of the range is approximately 3×10^9 m in magnitude and the maximum of the range acceleration is approximately 6×10^{-7} m/s^2 in magnitude.

To estimate the spectrum of the intersatellite observations, we use the mp.fft function in the Matlab Multiprecision Computing Toolbox [25] developed by ADVANPIX. By using the rectangular window, according to Eq. (11), the linear spectrum of the range L_{12}^{Sun} is estimated, as shown in Fig. 6. From Fig. 6, it can be seen that all the amplitudes above 8.8×10^{-23} m associated with the integer multiples of the orbital frequency may be estimated.

The capability of estimating the amplitudes in the range 8.8×10^{-23} m to 8.1×10^6 m is verified below. It is well known that when the eccentricity e of the orbit is smaller than the Laplace limit (which is about 0.6627), the position of the satellite may be expressed as a power series of e. Here, we consider the X-component of the orbit as an example. This term can be expressed in a series of the form [26]

$$X = X_{c0}(a,i,e,\Omega,w,M_0) + \sum_{k=1}^{\infty}[X_{ck}(a,i,e,\Omega,w,M_0)\cos knt + X_{sk}(a,i,e,\Omega,w,M_0)\sin knt], \quad (15)$$

where n is the orbital angular frequency, $X_{ck}(a,i,e,\Omega,w,M_0)$ and $X_{sk}(a,i,e,\Omega,w,M_0)$ are respectively the coefficients of $\cos(knt)$ and $\sin(knt)$. The linear spectrum at the kth multiples of the orbital frequency is in theory given by

$$LS_X(f_k = kf_0) = \sqrt{X_{ck}^2 + X_{sk}^2}, \quad k = 1, 2, \ldots. \quad (16)$$

Without loss of generality, we consider only the X-component of the position of satellite 1. The linear spectrum is estimated, as shown in Fig. 7. The theoretical value of the linear spectrum is also shown in Fig. 7. In Fig. 7, we present all the terms of the series that $k \leq 16$ in Eq. (16). The difference in the theoretical and estimated values of the linear spectrum is calculated and shown in Fig. 8. To clearly understand the difference, we also list the differences in Table V. From Table V, it can be seen that the maximum difference is approximately 7.5×10^{-24} m. Thus, it can be inferred that if the sampling is coherent, we may accurately estimate the amplitudes in the range 6.6×10^{-23}–1.49×10^{11} m in magnitude. Therefore, it can be inferred that the linear spectrum estimation of the simulated intersatellite range signal is highly reliable.

The linear spectrum of the range acceleration $\ddot{L}_{12}^{\mathrm{Sun}}$ is also estimated according to Eq. (11) using the rectangular

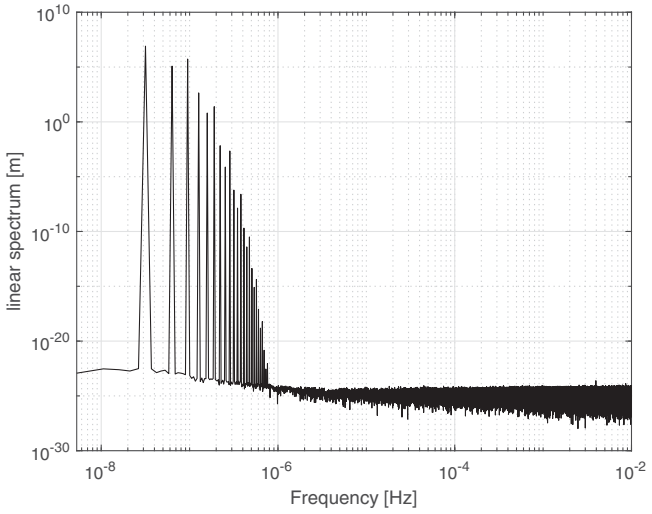

FIG. 6. Linear spectrum estimation of the range L_{12}^{Sun} between satellite 1 and 2 when only the central gravitational field of the Sun is considered in situation 1.

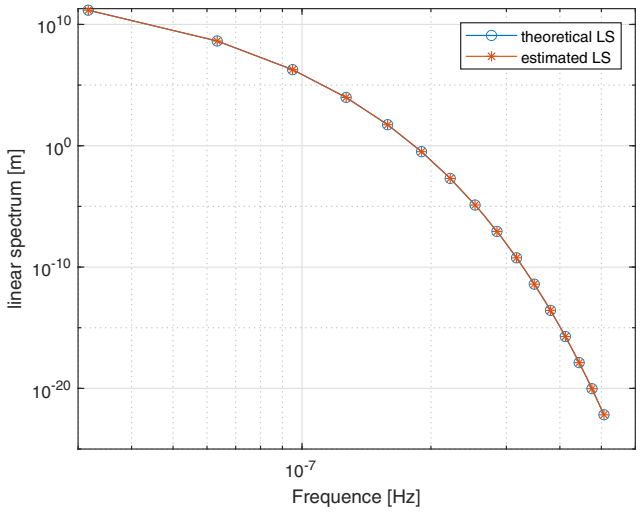

FIG. 7. The theoretical value (circle) and the estimated value (star) of the linear spectrum of the X-component of the position of satellite 1.

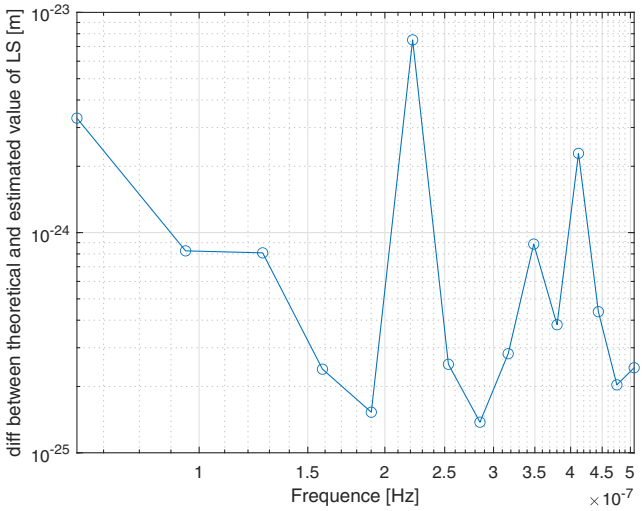

FIG. 8. The absolute value of the difference between the theoretical value and the estimated value of the linear spectrum of the X-component of the position of satellite 1.

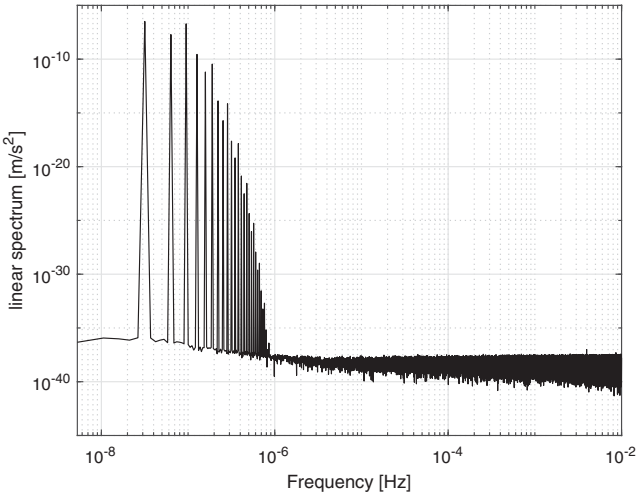

FIG. 9. Linear spectrum estimation of range acceleration $\dot{L}_{12}^{\mathrm{Sun}}$ between satellite 1 and satellite 2 when only the central gravitational field of the Sun is considered in situation 1.

window, and the same is shown in Fig. 9. From Fig. 9, it is clear that all the amplitudes above 3.9×10^{-37} m/s^2 are estimated, and from 8×10^{-7} Hz above in the frequency band, the estimation of the linear spectrum of the range acceleration is bounded by the numerical accuracy.

In the second situation, the sampling interval is set to $\Delta t = 50$ s, and the sampling duration is $N\Delta t$ where $N = [6T/\Delta t]$ is the largest integer, i.e., N = 3786983, such that $N\Delta t < 6T$.

When the rectangular window is used as that in situation 1, the linear spectrum of the intersatellite range L_{12}^{Sun} is estimated, as shown in Fig. 10. To illustrate the impact of noncoherent sampling, the linear spectrum estimation of L_{12}^{Sun} in situation 1 is also shown in Fig. 10. From Fig. 10, it can be seen that in situation 2, only the first six amplitudes associated with the first six multiples of the orbital frequency can be well estimated. The frequency components with amplitudes smaller than 0.3 m cannot be estimated. Thus, the noncoherent sampling has a significant impact on the spectral estimation.

For a more accurate spectral estimation, we must choose an appropriate window function. For the selection of window function, we need to consider several requirements: accuracy of the amplitude estimation, peak sidelobe level, decay rate, etc. Here, we consider the window functions of the form

TABLE V. The absolute value of the difference between the theoretical value and the estimated value of the linear spectrum of the X-component of the position of satellite 1.

Frequency	Difference (m)
f_0	0
$2f_0$	$3.308722450212110699485634768279851 \times 10^{-24}$
$3f_0$	$8.259689222026082007382962769936885 \times 10^{-25}$
$4f_0$	$8.090620552819114757247121103825478 \times 10^{-25}$
$5f_0$	$2.397685159225087536843772837108281 \times 10^{-25}$
$6f_0$	$1.528100499388421068153769956087734 \times 10^{-25}$
$7f_0$	$7.501270947435645429966724828186219 \times 10^{-24}$
$8f_0$	$2.523247864693961216172754610036539 \times 10^{-25}$
$9f_0$	$1.377291231064335447511938586139621 \times 10^{-25}$
$10f_0$	$2.818487843088533426788679629718897 \times 10^{-25}$
$11f_0$	$8.867036894584720284255704007236360 \times 10^{-25}$
$12f_0$	$3.813998971773728920589104835802704 \times 10^{-25}$
$13f_0$	$2.289576234173273516340985540293231 \times 10^{-24}$
$14f_0$	$4.373621447240115375992387282167479 \times 10^{-25}$
$15f_0$	$2.034121706875663642893762447701344 \times 10^{-25}$
$16f_0$	$2.433281991324140099685669910187225 \times 10^{-25}$

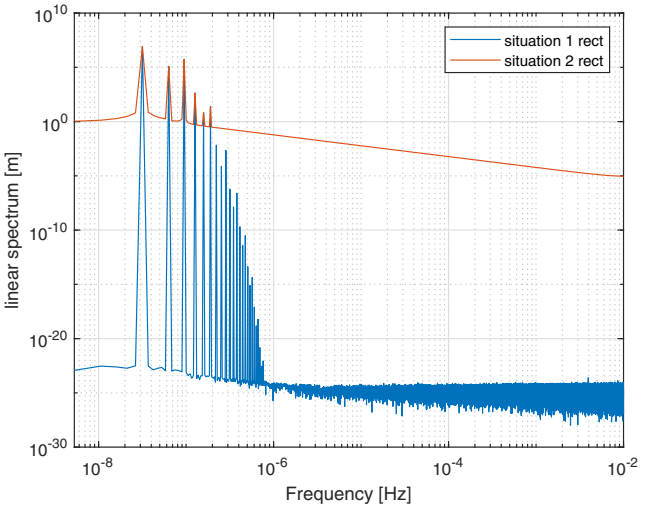

FIG. 10. Linear spectrum estimation for range L_{12}^{Sun} using the rectangular window when the sampling interval is set to 50 s.

$$w[n] = \sum_{k=0}^{M} a[k] \cos\left(-i2\pi \frac{nk}{M}\right), \quad n = 0, \ldots, N-1, \quad (17)$$

where $M+1$ is the number of coefficients of the window function. To obtain clearly visible peaks at two adjacent frequencies f_1 and f_2 (assume that $f_2 > f_1$), the frequency interval $f2-f1$ should satisfy the condition of $f2-f1 \geq 2(M+1)f_{\text{res}}$, or at least satisfy $f2-f1 \geq (M+1)f_{\text{res}}$ [27]. In this case, the minimum value of the interval between two frequency is the orbital frequency. The number of coefficients of the window function should be less than six. From the linear spectrum of situation 1, it is clear that the amplitudes decay very quickly. Therefore, to suppress the leakage effect of low frequency components on high frequency components, there are tight requirements on the peak sidelobe level and decay rate. Given these requirements, a window of five coefficients (i.e., 5-FD) [28] with lower peak sidelobe level and fast decay rate is introduced to estimate the linear spectrum in situation 2. This window function is defined by [28]

$$w[z] = 0.2734375 - 0.4375\cos(z) + 0.21875\cos(2z) - 0.0625\cos(3z) + 0.0078125\cos(4z). \quad (18)$$

By using the window function defined in Eq. (18), the linear spectrum of the armlength L_{12}^{Sun} is estimated and shown in Fig. 11. The linear spectrum of L_{12}^{Sun} in situation 1 is also shown in Fig. 11 for the purpose of comparison. We see that the amplitudes above 1×10^{-12} m are well estimated.

The linear spectrum of the range acceleration $\ddot{L}_{12}^{\text{Sun}}$ in situation 2 is also estimated using the 5-FD window function, as shown in Fig. 12. We have indicated the result

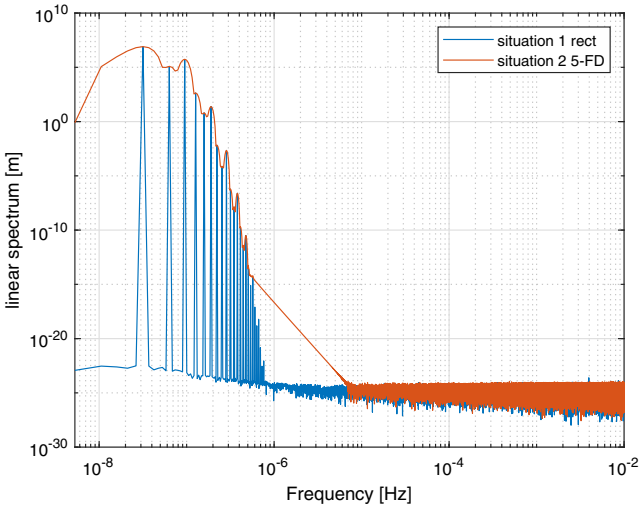

FIG. 11. Linear spectrum estimation for range L_{12}^{Sun} using the 5-FD window function when the sampling interval is set to 50 s.

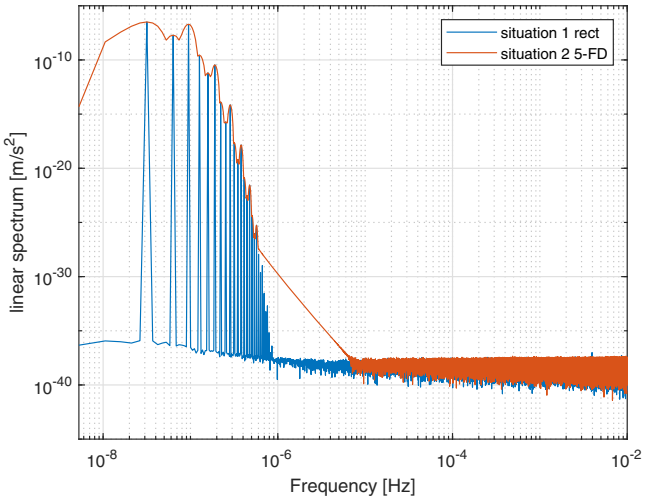

FIG. 12. Linear spectrum estimation for range acceleration $\ddot{L}_{12}^{\text{Sun}}$ using the 5-FD window function when the sampling interval is set to 50 s.

in Fig. 9 in the same figure for an easier comparison. It can be seen that the amplitudes above 1×10^{-26} m/s^2 are well estimated.

C. Effect of major bodies in the solar system

In this section, we will analyze the influences of the major bodies on the intersatellite observation of the Taiji mission. The equation of motion of the satellite is described by Eq. (9). The duration of the integration time is from January 1, 2030, to January 1, 2036, and the sampling interval is set to 50 s. The equation of motion is solved using DOP853 based on 34 significant digits, and the verification of the accuracy of integration is as presented in Sec. III B. Using the initial conditions shown in Table IV, we can integrate from Eq. (9) the states of the satellites, and then determine the range and range acceleration according to Eqs. (1) and (3), respectively.

The time series of range L_{12} and range acceleration $\ddot{L}_{12}$ between satellite 1 and satellite 2 are shown in Figs. 13 and 14, respectively. From Figs. 13 and 14, it is clear that the maximum values of L_{12} and $\ddot{L}_{12}$ are about 3×10^9 m and 2×10^{-6} m/s^2 in magnitude, respectively.

It is easy to infer from Figs. 13 and 14 that the orbit is not strictly periodic. This will lead to more serious leakage during the spectrum estimation of L_{12} and $\ddot{L}_{12}$. Because of the limitations of the finite sampling duration, it is difficult to achieve highly accurate spectrum estimation, and thus, we seek to give an upper bound estimation of power spectrum of the signals.

Based on the window function defined by Eq. (18), the linear spectrum of L_{12} is estimated according to Eq. (11). The result is shown in Fig. 15, where the red solid line represents the linear spectrum of L_{12}. In Fig. 15, due to leakage, the peaks at orbital frequencies can still be

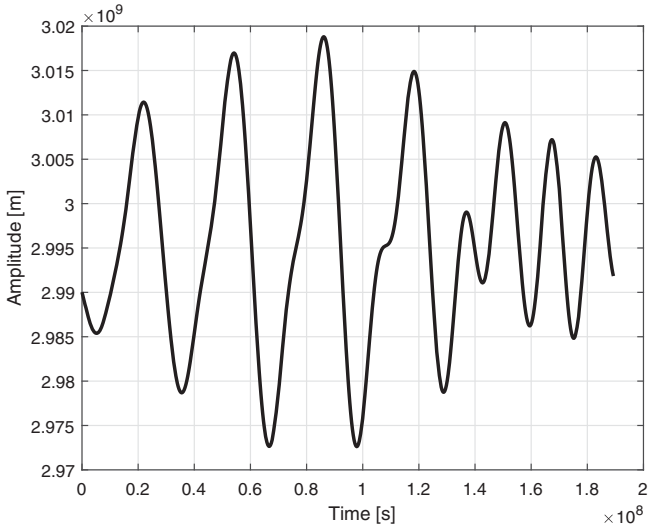

FIG. 13. Simulated time series of L_{12}.

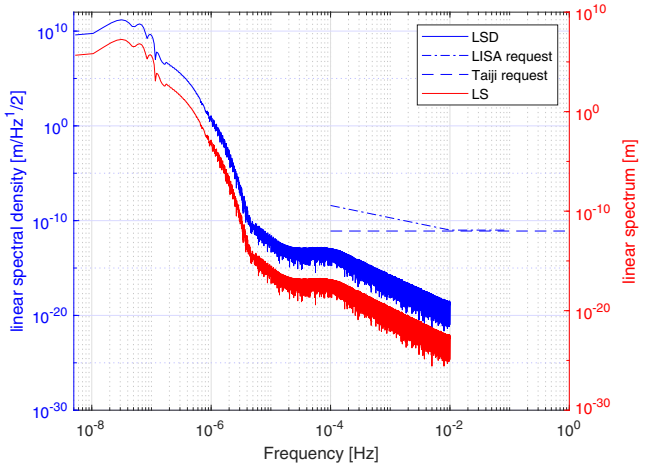

FIG. 15. Linear spectrum (the red solid line) and linear spectral density (the blue solid line) estimation for range L_{12}, using the 5-FD window function. Total influence of gravitational fields of the Sun and ten other major bodies are considered.

estimated but they are no longer as pronounced as those when only the gravitational field of the Sun is considered. From Fig. 15, it can be easily seen that in the frequency band 1×10^{-6}–4×10^{-6} Hz, the upper bound of the linear spectrum are determined by the decay rate of the window function, which is approximately 1×10^{-3} m at 1×10^{-6} Hz, and it then decreases to about 4×10^{-14} m at 4×10^{-6} Hz. In the frequency band 4×10^{-6}–0.01 Hz, the linear spectrum is actually constrained because of the numerical accuracy; the value is smaller than 1×10^{-14} m.

To analyze the impact of the armlength generated by the gravitational fields of the major bodies in the detection frequency, we also calculate the linear spectral density of L_{12}. Based on the window function defined by Eq. (18), the linear spectral density of L_{12} is estimated according to Eq. (13). The result is shown in Fig. 15, where the blue solid line represents the linear spectral density of L_{12}. In Fig. 15, we also plot the requirement of Taiji (blue dashed line) for the range, as shown in Table I, and the requirement of LISA (blue dash-dot line) for the range. For the LISA mission, the requirement for the ranging noise is [6]

$$S_{IFO}^{1/2} \leq 10 \times 10^{-12} \frac{m}{\sqrt{\text{Hz}}} \cdot \sqrt{1 + \left(\frac{2\ \text{mHz}}{f}\right)^4},$$
$$0.1\ \text{mHz} \leq f \leq 0.1\ \text{Hz}. \tag{19}$$

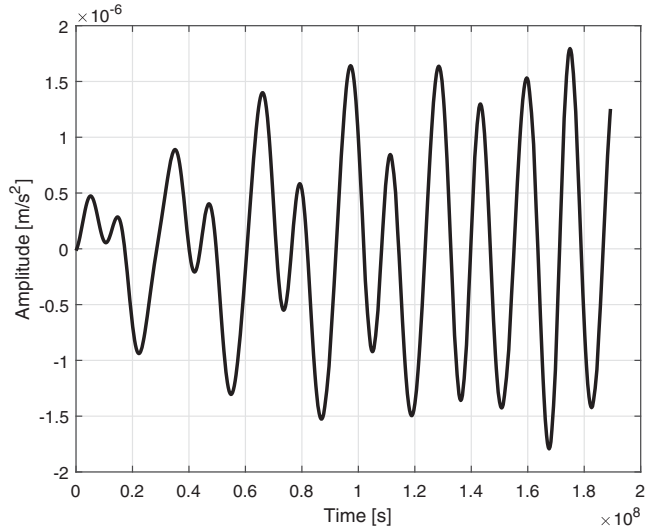

FIG. 14. Simulated time series of $\ddot{L}_{12}$.

According to Fig. 15, the intersatellite range due to major bodies in the solar system is dominant in the very low-frequency band. However, it decreases rapidly when the frequency becomes larger, and its value is nearly 1×10^{-13} m/$\sqrt{\text{Hz}}$ at 0.1 mHz. Because the result may be seen as an upper bound, we numerically verify that the impact of the gravitational field of major bodies in solar system on the range L_{12} for both the Taiji and LISA missions may be neglected in the detection frequency band.

To estimate the linear spectrum of $\ddot{L}_{12}$, we still use the 5-FD window function. The result is shown in Fig. 16, where the red solid line represents the linear spectrum of $\ddot{L}_{12}$. To study the impact in the range acceleration generated by the gravitational fields of the major bodies in the detection frequency, we also calculate the linear spectral density of $\ddot{L}_{12}$. Based on the window function defined by Eq. (18), the linear spectral density of $\ddot{L}_{12}$ is estimated according to Eq. (13). The result is shown in Fig. 16, where the blue solid line represents the linear spectral density of $\ddot{L}_{12}$. In Fig. 16, where we also plot the requirement of the range acceleration of Taiji (blue dashed line) as shown in Table I and of LISA (blue dash-dot line). For the LISA mission, the requirement for the ranging acceleration noise is given by [6]

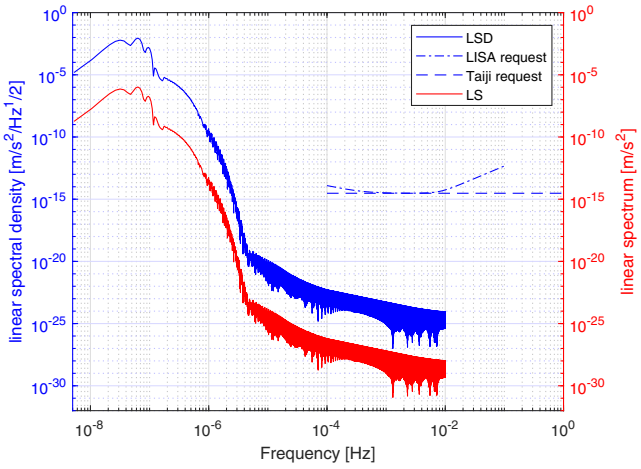

FIG. 16. Linear spectrum (the red solid line) and linear spectral density (the blue solid line) estimation for range acceleration $\ddot{L}_{12}$, using the 5-FD window function. Total influence of gravitational fields of the Sun and ten other major bodies are considered.

$$S_a^{1/2} \le 3\times 10^{-15}\frac{m/s^2}{\sqrt{\mathrm{Hz}}}\cdot\sqrt{1+\left(\frac{0.4\ \mathrm{mHz}}{f}\right)^2}\cdot\sqrt{1+\left(\frac{f}{8\ \mathrm{mHz}}\right)^4},\quad 0.1\ \mathrm{mHz}\le f\le 0.1\ \mathrm{Hz}, \tag{20}$$

According to Fig. 16, the intersatellite range acceleration because of major bodies in the solar system is dominant in the very low-frequency band. However, it decreases rapidly when the frequency becomes larger, and its value is nearly $5\times 10^{-23}\ \mathrm{m/s^2/\sqrt{Hz}}$. Similar to the result of the analysis of range, the impact of the gravitational field of the major bodies in solar system on the range acceleration $\ddot{L}_{12}$ for both the Taiji and LISA missions may be neglected in the detection frequency band.

Because the spectral estimation results for the other two arms are similar to those for the arm between satellites 1 and 2, they are not shown in this paper.

In the latter part of the study, we will also estimate the linear spectrum and the linear spectral density of the relative acceleration along the line-of-sight direction of the two satellites caused by each celestial body alone. The relative acceleration of the pth body along the line of sight between satellite 1 and satellite 2 may be calculated as follows:

$$a_{12,p} = \frac{\vec{r}_2-\vec{r}_1}{L_{12}}\cdot(\vec{a}_{2,p}-\vec{a}_{1,p}), \tag{21}$$

where $\vec{a}_{1,p}$ and $\vec{a}_{2,p}$ represent the gravitational accelerations of the pth body on satellite 1 and satellite 2, respectively.

Based on the 5-FD window function defined in Eq. (18), the linear spectrum of the relative accelerations $a_{12,p}$ of each body is estimated, as shown in Fig. 17. The linear spectrum of the total relative acceleration $\sum_p a_{12,p}$ of all bodies is also shown in Fig. 17. The linear spectral density is also estimated, as shown in Fig. 18. The linear spectral density of the total relative acceleration $\sum_p a_{12,p}$ of all bodies is also shown in Fig. 18. From Fig. 17, it can be seen from the comparison of the total relative acceleration with the relative acceleration of each body, the total relative acceleration may be slightly smaller than the relative acceleration from some single body in a special band. For example, in the vicinity of the two multiples of the orbital frequency, the total acceleration is slightly smaller than that of Earth, which means that there may be cancellation among the relative accelerations of the celestial bodies. However, from Fig. 17, it can also be easily seen that the distribution of the relative acceleration

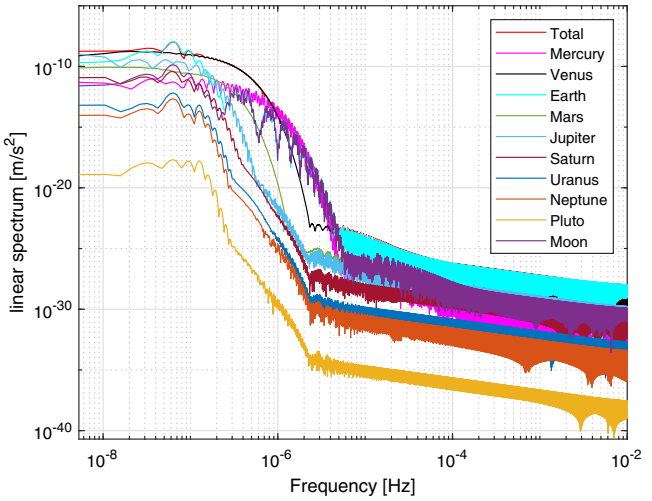

FIG. 17. Linear spectrum estimation for line-of-sight relative acceleration $a_{12,p}$ caused by each celestial body.

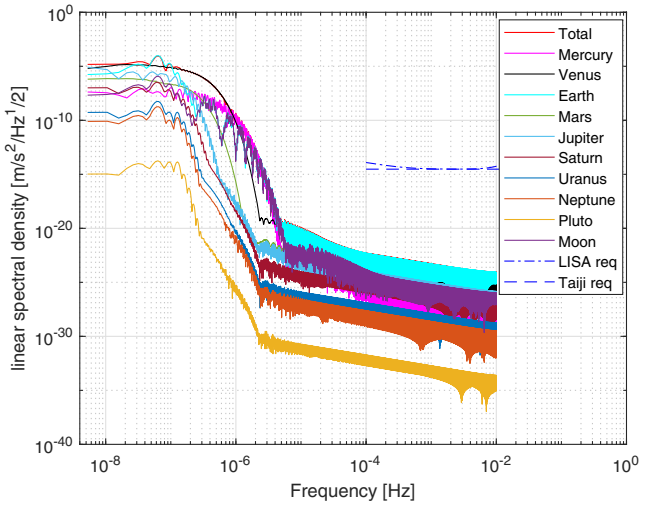

FIG. 18. Linear spectral density estimation for line-of-sight relative acceleration $a_{12,p}$ caused by each celestial body.

caused by each major body in frequency domain. According to the contribution of each major body to the total accelerations at the low frequency band in the range 3.17×10^{-8}–1×10^{-7} Hz, we may sort by value from largest to smallest: the Earth, Venus, Jupiter, Mars, Moon, Saturn, Mercury, Uranus, Neptune, and Pluto. To clearly see the contribution of each major body in the frequency band 1×10^{-7}–3×10^{-6} Hz, we refer to the paragraph from Fig. 17, which is shown in Fig. 19. From the figure, it can be seen that although the contribution from Earth in time domain is the largest (see Fig. 20), in frequency domain, the Earth contributes the most in the frequency band 3.17×10^{-8}–1×10^{-7} Hz and Venus contributes the most in 1×10^{-7}–8×10^{-7} Hz, and Mercury contributes the most in 8×10^{-7}–3×10^{-6} Hz.

The same result may be seen from Fig. 18 mainly because the LSD is proportional to the LS.

The motion of the Moon relative to the Earth can be approximated as a periodic motion, the period of which is a synodic month ($\approx 3.92 \times 10^{-7}$ Hz). Thus, in principle, the Earth-Moon system will induce a resonance and a series of periodic perturbations with frequencies equal to harmonics of the synodic month. From Fig. 19, it can be easily seen that the relative acceleration caused by Earth and Moon has peaks at the first seven harmonics of the synodic month, thus the results from the numerical simulation are consistent with those from the theoretical analysis. However, in 3.92×10^{-7}–8×10^{-7} Hz and 8×10^{-7}–2.74×10^{-6} Hz, Venus and Mercury have larger impacts than Earth-Moon system, respectively. Therefore, the impact of Earth-Moon system cannot be clearly seen from the linear spectrum of L_{12} when the gravity of all celestial bodies are included in the force, which is easily to be seen in Fig. 15.

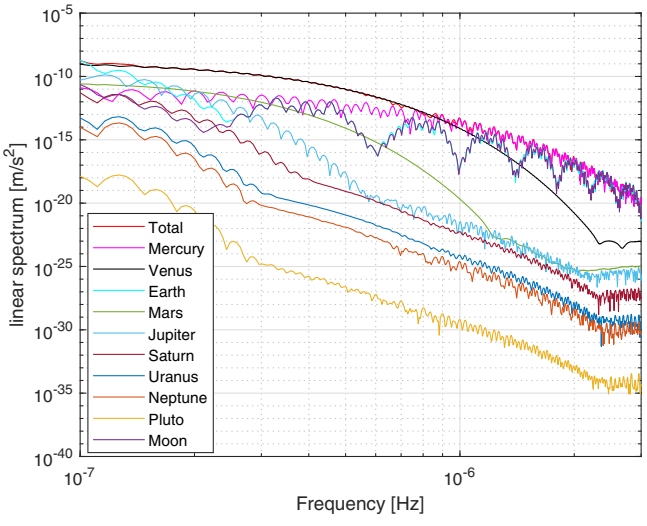

FIG. 19. Local magnification of linear spectrum estimation for line-of-sight relative acceleration $a_{12,p}$ caused by each celestial body.

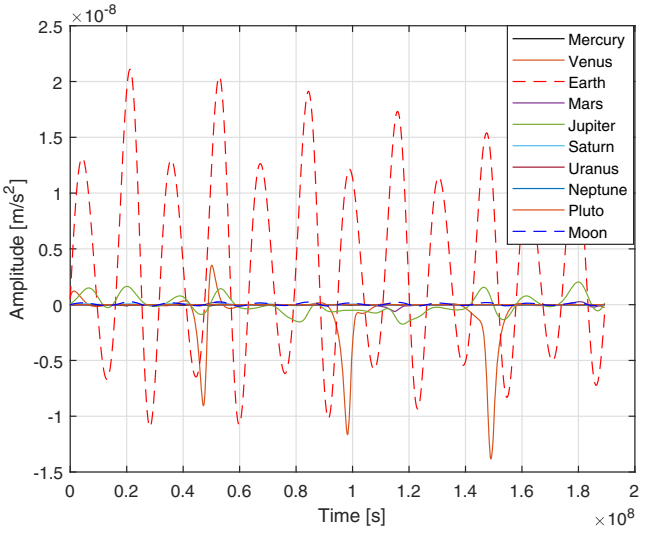

FIG. 20. Simulated time series of line-of-sight relative acceleration $a_{12,p}$ caused by each celestial body.

D. Effect of small celestial bodies

Finally, we discuss the combined effect of the gravitational fields of the 344 asteroids outlined in JPL DE430 on the relative acceleration along the line of sight between two satellites. The relative acceleration $a_{12,\mathrm{ast}}$ along the line of sight between satellites 1 and 2 is calculated according to Eq. (21), where $\vec{a}_{1,\mathrm{ast}}$ and $\vec{a}_{2,\mathrm{ast}}$ represent the accelerations of satellite 1 and satellite 2 because of the 344 asteroids, respectively. The time series $a_{12,\mathrm{ast}}$ is calculated, as shown in Fig. 21. The linear spectrum (the red solid line) and linear spectral density (the blue solid line) are estimated, as shown in Fig. 22. From Fig. 21, it can be seen that the total contribution of the gravitational fields of these asteroids to $a_{12,\mathrm{ast}}$ is smaller than 1.5×10^{-14} m/s^2 in magnitude. From

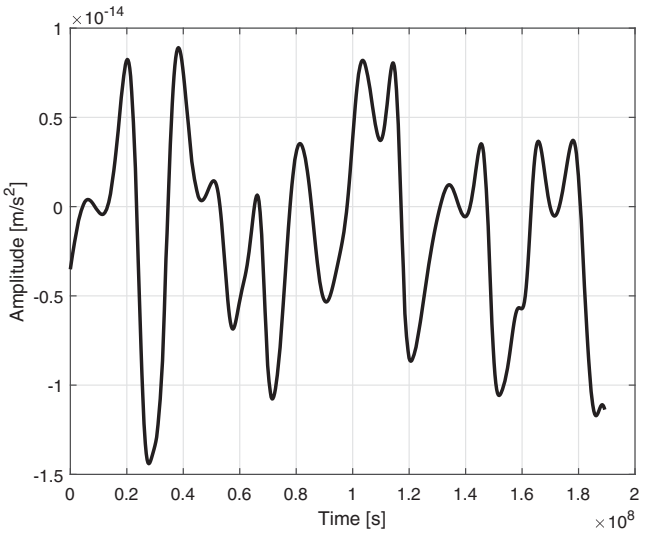

FIG. 21. Simulated time series of $a_{12,\mathrm{ast}}$ jointly caused by 344 asteroids outlined in JPL DE430.

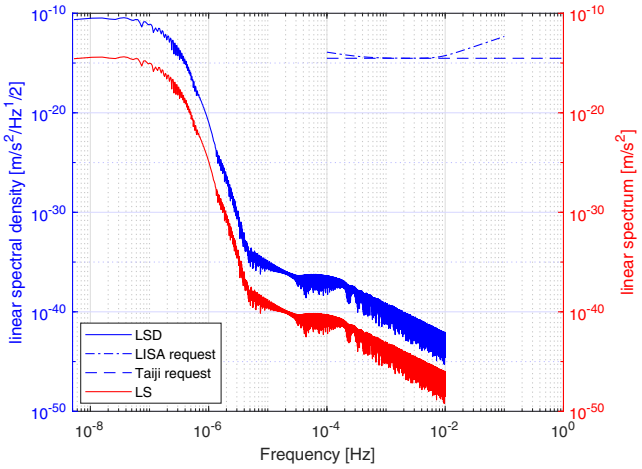

FIG. 22. Linear spectrum (the red solid line) and linear spectral density (the blue solid line) estimation of $a_{12,\mathrm{ast}}$ jointly caused by 344 asteroids outlined in JPL DE430.

Fig. 22, it can be clearly seen that the total influence of the 344 asteroids outlined in JPL DE430 is significantly less compared to the limits required by either Taiji or LISA.

Likewise, the spectral estimations for the other two arms are similar to that for $a_{12,\mathrm{ast}}$, and thus they are no longer shown in this paper.

V. CONCLUSION

This paper presents a detailed analysis of whether disturbances due to the gravitational fields of the major celestial bodies in the solar system affect the detection of gravitational waves in the sensitive frequency band of the Taiji mission. To resolve this question, a high-precision orbit propagator capable of producing accuracies of approximately 0.03 pm in scales of 1 AU is first developed. With this propagator, the range and range acceleration between two satellites due to the gravitational fields of celestial bodies are then simulated. Through the use of fast Fourier transform with the suitable window function, the linear spectrum and linear spectral densities of the range and range acceleration are analyzed. Given the base requirements of the Taiji mission for the noises of range and range acceleration, and based on the results obtained for the linear spectral densities, we determine that the influences of the gravitational fields of the celestial bodies are considerably lower than the corresponding limits for noise required by the Taiji mission. The low level of the orbital perturbation from solar system bodies shown here means that the subtraction of the perturbation from a LISA / Taiji data series is not necessary. With the promise that Taiji offers for the progression of science and technology, we hope our study would constitute foundational knowledge for the detection of gravitational waves in the heliocentric orbit through Taiji, LISA, and similar missions, particularly going to lower frequencies. Such as some missions presented in the ESA Voyage 2050 program [29] which go beyond the LISA low band edge of 100 μHz to reach μHz and lower frequencies where such gravitational perturbations may be more important.

ACKNOWLEDGMENTS

The present research is supported by the China National Key R&D Program "detection of the gravitational waves" (Grant No. 2020YFC2201300 and No. 2021YFC2202900), National Natural Science Foundation of China (Grant No. 11905244). We would like to thank Editage (www.editage.cn) for English language editing.

[1] Wen-Rui Hu and Yue-Liang Wu, The Taiji Program in Space for gravitational wave physics and the nature of gravity, Nat. Sci. Rev. **4**, 685 (2017).
[2] Ziren Luo, ZongKuan Guo, Gang Jin, Yueliang Wu, and Wenrui Hu, A brief analysis to Taiji: Science and technology, Results Phys. **16**, 102918 (2020).
[3] Gong Xue-Fei, Xu Sheng-Nian, Yuan Ye-Fei, Bai Shan, Bian Xing, Cao Zhou-Jian, Chen Ge-Rui, Dong Peng, Gao Tian-Shu, Gao Wei *et al.*, Laser interferometric gravitational wave detection in space and structure formation in the early universe, Chin. Astron. Astrophys. **39**, 411 (2015).
[4] B. L. Schumaker, Overview of disturbance reduction requirements for LISA, *Proceedings of the 4th International LISA Symptoms, Pennsylvania, 2002* (2002).
[5] Bonny L. Schumaker, Disturbance reduction requirements for LISA, Classical Quantum Gravity **20**, S239 (2003).
[6] Pau Amaro-Seoane, Heather Audley, Stanislav Babak *et al.*, Laser interferometer space antenna, arXiv:1702.00786.
[7] Toru Yoshizawa, *Handbook of Optical Metrology: Principles and Applications* (CRC Press, 2009), 10.1201/b18328.
[8] Simon Barke, *Inter-Spacecraft Frequency Distribution for Future Gravitational Wave Observatories* (Gottfried Wilhelm Leibniz Universität Hannover, Hannover, 2015).
[9] Jiafeng Zhang, Zhen Yang, Xiaoshan Ma, Xiaodong Peng, Heshan Liu, Wenlin Tang, Mengyuan Zhao, Chen Gao, Li-E Qiang, Xiaoqing Han *et al.*, Inter-spacecraft offset frequency setting strategy in the Taiji program, Appl. Opt. **61**, 837 (2022).
[10] W. M. Folkner, P. L. Bender, and R. T Stebbins, LISA mission concept study, laser interferometer space antenna for the detection and observation of gravitational waves, Technical Report No. JPL-Publ-97-16, 1998.

[11] Z. R. Luo, S. Bai, X. Bian, G. Chen, P. Dong, Y. Dong *et al.*, Space laser interferometry gravitational wave detection, Adv. Mech. **43**, 415 (2013).
[12] Massimo Cerdonio, Fabrizio De Marchi, Roberto De Pietri, Philippe Jetzer, Francesco Marzari, Giulio Mazzolo, Antonello Ortolan, and Mauro Sereno, Modulation of LISA free-fall orbits due to the Earth–Moon system, Classical Quantum Gravity **27**, 165007 (2010).
[13] Florian Wöske, T. Kato, M. List, and B. Rievers, Development of a high precision simulation tool for gravity recovery missions like grace, Advances in Astronautical Sciences **158**, 2445 (2016).
[14] Xuefeng Zhang, Chengjian Luo, Lei Jiao, Bobing Ye, Huimin Yuan, Lin Cai, Defeng Gu, Jianwei Mei, and Jun Luo, Effect of Earth-Moon's gravity on Tianqin's range acceleration noise, Phys. Rev. D **103**, 062001 (2021).
[15] MPFR C++, http://www.holoborodko.com/pavel/mpfr/.
[16] Roger Alexander, Solving ordinary differential equations I: Nonstiff problems (E. Hairer, S. P. Norsett, and G. Wanner). SIAM Rev. **32**, 485 (1990).
[17] William M. Folkner, James G. Williams, Dale H. Boggs, Ryan S. Park, and Petr Kuchynka, The planetary and lunar ephemerides DE430 and DE431, Interplanet. Netw. Prog. Rep. **42**, 1 (2014).
[18] Shen Yunzhong, Algorithm characteristics of dynamic approach-based satellite gravimetry and its improvement proposals, Acta Geod. Cartogr. Sin. **46**, 1308 (2017).
[19] Yufeng Nie, Yunzhong Shen, Qiujie Chen, and Yun Xiao, Hybrid-precision arithmetic for numerical orbit integration towards future satellite gravimetry missions, Adv. Space Res. **66**, 671 (2020).
[20] Ilias Daras, Roland Pail, Michael Murböck, and Weiyong Yi, Gravity field processing with enhanced numerical precision for LL-SST missions, J. Geod. **89**, 99 (2015).
[21] D. Curtis Howard, *Orbital Mechanics for Engineering Students (Fourth Edition)* (Butterworth-Heinemann, 2021), pp. 181–229.
[22] Kyle T. Alfriend, Srinivas R. Vadali, Pini Gurfil, Jonathan P. How, and Louis Breger, *Spacecraft Formation Flying: Dynamics, Control and Navigation* (Elsevier, New York, 2009), Vol. 2.
[23] Wenlin Tang, Preliminary study of the orbit design of the Chinese mission to detect the gravitational wave in space, Ph.D. thesis, Chinese Academy of Sciences University, 2014.
[24] Gerhard Heinzel, Albrecht Rüdiger, and Roland Schilling, Spectrum and spectral density estimation by the discrete fourier transform (DFT), including a comprehensive list of window functions and some new at-top windows, Max Planck Institute, 2002.
[25] Multiprecision computing toolbox for matlab, https://www.advanpix.com/.
[26] Lin Liu and Xiyun Hou, *Fundamentals of Orbital Dymanics (In Chinese)* (Higher Education Press, 2018), ISBN: 9787040487428.
[27] Luigi Salvatore and Amerigo Trotta, Flat-top windows for PWM waveform processing via DFT, in *IEE Proceedings B (Electric Power Applications)* (IET, 1988), Vol. 135, pp. 346–361.
[28] Shuping Song, Hongzhong Ma, Gang Xu, Fuzong Wang, and Jie Wang, Five-term maximum sidelobe attenuation window interpolation power harmonic analysis, Automation of Electric Power Systems **39**, 83 (2015).
[29] Alberto Sesana *et al.*, Unveiling the gravitational universe at μ-Hz frequencies, Exp. Astron. **51**, 1333 (2021).